

Alternation of the flickering morphology between the high and low state in MV Lyr

A. Dobrotka¹, H. Negoro² and P. Konopka³

¹ Advanced Technologies Research Institute, Faculty of Materials Science and Technology in Trnava, Slovak University of Technology in Bratislava, Bottova 25, 917 24 Trnava, Slovakia

² Department of Physics, Nihon University, 1-8 Kanda-Surugadai, Chiyoda-ku, Tokyo 101-8308, Japan

³ Komenského 4530/6, 92101 Piešťany, Slovakia

Received / Accepted

ABSTRACT

Aims. We studied unique data of a nova-like system MV Lyr during transition from the high to low state and vice versa taken by the *Kepler* space telescope. We were interested in evolution of frequency components found previously by Scaringi et al. in different data also obtained by *Kepler*.

Methods. We divided the light curve into 10 day segments and investigated the corresponding power density spectra. We searched for individual frequency components by fitting with Lorentzian functions. Additionally, we investigated the variability using averaged shot profiles calculated from the light curve divided into 10 equally spaces subsamples.

Results. We found very complex changes of the power density spectra. We focused our study onto three frequency components. Strong activity increase is seen at low frequencies. Contrariwise, the high frequency part of the spectrum strongly decreases in power with specific rise in characteristic frequencies of the individual components. We discuss various scenarios of this phenomenology as reprocessing of X-rays in a receding accretion disc or a radiation from a more active region at the outer disc. Finally, we show that various cataclysmic variables show similar characteristic frequencies in their power density spectra. These are dependent on activity stage, making the situation similar to X-ray binaries.

Key words. accretion, accretion discs - Stars: dwarf novae - stars: individual: MV Lyr - Stars: novae, cataclysmic variables - X-rays: binaries

1. Introduction

A great variety of objects such as cataclysmic variables (CVs) are powered by accretion process. It is based on mass loss from a companion star. The transported gas falls towards the central compact object being a white dwarf, and in the absence of a strong magnetic field, an accretion disc forms. The same model is valid also for related objects as X-ray binaries (see e.g. Warner 1995 or Frank et al. 1992 for a review). The main difference is that the latter has a neutron star or a black hole instead of the white dwarf.

The family of CVs is divided into several subclasses based on characteristic variability patterns. Dwarf novae show quasiregular outbursts with durations of several days and appearing on a time scale of 10 - 100 days (see Warner 1995 for review). Nova-like or VY Scl systems spend most of their life time in a high state while they sporadically exhibit transition into a low brightness state. This behaviour can be connected to changes in accretion rate. In this way, the duration of the high states in VY Scl systems and dwarf novae is significantly different. It is relatively stable and long lasting for the former, while it is only temporary for the latter (outbursts). The shorter durations of the dwarf novae high state can be explained by the limited amount of gas in the depletive disc driving the outburst. The latter is a con-

sequence of a mass accretion rate being unstable because of hydrogen ionization. This phenomenon is well explained by the so called disc instability model (see Lasota 2001 for review). Meanwhile, in VY Scl systems, the mass accretion rate remains above the critical limit required for stability, explaining the longer duration of high states. The low state is generated by a sudden drop/stop of mass transfer from the secondary (King & Cannizzo 1998, Hessman 2000).

The existence of the accretion process is usually seen as fast stochastic variability (a.k.a. flickering). Flickering has three very basic observational characteristics; 1) linear correlation between variability amplitude and log-normally distributed flux (so called rms-flux relation) observed in all variety of accreting systems (see e.g. Scaringi et al. 2012b, Van de Sande et al. 2015 for CVs case), 2) character of red noise or band limited noise with characteristic frequencies in power density spectra (PDS, see e.g. Scaringi et al. 2012a, Dobrotka et al. 2014, Dobrotka et al. 2016 for CVs case) and 3) time lags where flares reach their maxima slightly earlier in the blue than in the red (Scaringi et al. 2013, Bruch 2015)

An alternative method to "see" the PDS components was proposed by Negoro et al. (1994). The authors superposed many flares (shots) from the *Ginga* light curve of the X-ray binary Cyg X-1 in order to get a mean profile showing all typical stable feature like the central spike and two humps on both sides of the spike. A very similar pro-

Send offprint requests to: A. Dobrotka, e-mail: andrej.dobrotka@stuba.sk

file was found by Sasada et al. (2017) using *Kepler* data of the blazar W2R 1926+42 but on a much longer time scale. The third object showing such a multicomponent flare shape with a central spike and side-lobes is MV Lyr (Dobrotka et al. 2019) with a time scale between the X-ray binary and the blazar. All three findings make the situation very interesting because of very different nature of all three objects. Especially the radiation origin in the blazar is very different from the other two objects.

MV Lyr is a well studied bright nova-like system ideal for flickering study consisting of two phases, i.e. before and after the *Kepler* space telescope. During the former, several studies suggested various variability components. Besides coherent frequencies close to $\log(f/\text{Hz}) = -4.08$ Borisov (1992) and Skillman et al. (1995) reported a possible quasi periodic oscillation (QPO) at approximately $\log(f/\text{Hz}) = -3.45$. Kraicheva et al. (1999) also found a QPO at a similar frequency. First detection of the linear rms-flux relation was presented by Boeva et al. (2011). The latter got an unambiguous shape using extensive *Kepler* data in the study of Scaringi et al. (2012b). Scaringi et al. (2012a) used the same *Kepler* data to study the PDS morphology. The authors reported a multicomponent nature with four different characteristic frequencies. Some of these components were close to the previously detected signals. Time lags study in different bands was performed by Scaringi et al. (2013) using ULTRACAM on the William Herschel Telescope. For MV Lyr 3 s lags are observed at the lowest frequencies with redder bands lagging the bluer ones. The authors suggest reprocessing of the X-ray photons on to the accretion disc or inside-out shocks traveling within the disc as explanation for the observed lags. Scaringi (2014) presented a sandwich model as responsible for the highest PDS component in which the central geometrically thin disc is surrounded by a geometrically thick disc (hot corona). This model was confirmed by direct X-ray observations by Dobrotka et al. (2017).

The localization of the individual PDS components is not trivial and various attempts have been made. Besides the modeling of Scaringi (2014), a shot noise model of Dobrotka et al. (2015) yields very similar results to the former, i.e. the radius of the highest frequency component emission region of approximately 10^{10} cm, and high α parameter (Shakura & Sunyaev 1973) value (close to 1). Moreover, supposing α values from 0.1 to 0.4 the two lower PDS components were localized into the geometrically thin disc and a more active outer disc rim.

The shot noise model is too strong simplification of the real physics, and the localization of the PDS components except the highest one based on Scaringi (2014) and Dobrotka et al. (2017) is still not certain. Therefore, observational studies are very useful, mainly during dynamic stages of the accretion disc. *Kepler* data of MV Lyr comprise such transition to/from the low state typical for nova-like systems (probably) caused by disc reformation. Therefore, we can follow the disc regression and subsequent reconstruction together with PDS evolution during such a high/low state transition. This can yield different flickering source identification and better understanding of the accretion flow geometry or structure of the accretion disc. In this paper we perform detailed analysis of the mentioned activity stage transition of MV Lyr observed by the *Kepler* satellite.

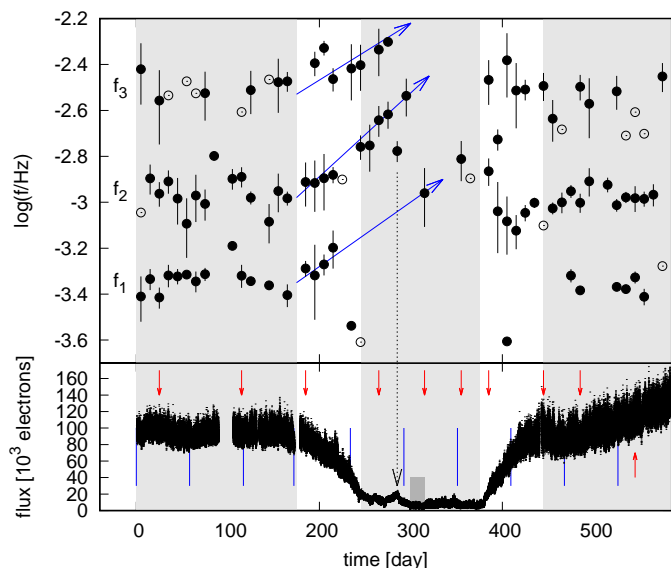


Fig. 1. Upper panel - the (time) evolution of PDS components derived using Lorentzians in Eq. (1). The characteristic frequencies f_i (marked as labels on the left side) are shown by the black circles with error bars ($\delta\log(f_i)$) for significantly detected components with $\delta\log(f_i) < 0.2$, and by black circles without error bars for less significantly detected ones with $0.2 < \delta\log(f_i) < 0.5$. The light shaded areas show time intervals selected as before, during and after the low state. Blue arrows outlines possible frequency evolution, and dashed vertical black arrow shows the connection of one deviated point with local re-brightening (see text for details). Lower panel - the analyzed light curve for comparison. The red arrows show the (middle) time location of the PDS examples in Fig. 4. The dark shaded area is the deep low state identified by Scaringi et al. (2017) (see Section 4 for details). The vertical blue lines divide the light curve into 10 equally spaced subsamples for shot profile calculation in Section 4.

2. Data

The data analyzed in this work represent the evolution of MV Lyr from the most common high state to a minimum and back. The data are taken by the *Kepler* satellite (Borucki et al. 2010) with a cadence of approximately 60 s. The studied light curve lasts approximately 585 days. *Kepler* data comprise relatively many rare null point which we removed. No other correction was needed. The bottom panel of Fig. 1 depicts this light curve divided into three intervals marked as shaded areas, i.e. before, during and after the low state.

3. PDS analysis

3.1. Method

Based on our motivation to study the PDS evolution from the high to low state (and vice versa), we divided the light curve from Fig. 1 into equally spaced segments with duration of 10 days. Every segment is divided into ten subsamples, and a periodogram is calculated from each subsample using the Lomb-Scargle algorithm¹ Scargle (1982). All pe-

¹ *Kepler* data are full of gaps, rare null points and interval of these null points. Therefore, the Lomb-Scargle method is suitable because it is designed for such unevenly spaced data. Otherwise discrete Fourier transform would be ideal.

riodograms (power² p as function of frequency f) were subsequently transformed into $\log(f)$ - $\log(p)$ space, because of several reasons. Firstly, Papadakis & Lawrence (1993) concluded that for examination of variations of the PDS with time (to detect QPOs), the periodogram averaging in logarithm is better rather than averaging the periodograms themselves. Secondly, such averaging of $\log(p)$ yields symmetric errors (see e.g. van der Klis 1989, Aranzana et al. 2018). Thirdly, the whole $\log(f)$ interval of the PDS is rebinned with a constant frequency step of 0.05, and such frequency bins comprise more and more periodogram points toward higher frequencies. The PDS scatter rises toward higher frequencies when binned with a constant frequency step in a linear scale (Fig. 4 of Scaringi et al. 2012a), and any potential frequency component above $\log(f/\text{Hz}) = -3$ is totally buried and non detectable. Finally, all $\log(p)$ points within each frequency bin were averaged³, with the standard error of the mean as an uncertainty estimate. Such PDS estimate has equal resolution in the whole $\log(f)$ interval (see e.g. Shahbaz et al. 2005, Aranzana et al. 2018).

The periodogram averaging and binning lower the PDS scatter, while the light curve division determines the frequency resolution being equal to the lowest PDS frequency (before re-binning). The latter is proportional to the shortest light curve subsample duration. Therefore, an empirical compromise between noise and resolution must be found. The high frequency PDS end is set up empirically. Usually it is equal to the frequency where Poisson noise becomes dominant so that the PDS becomes flat (white noise) with no additional information. We concentrated our study to the high frequency part of the PDS, i.e. we excluded the two lowest (from total of four) PDS components detected by Scaringi et al. (2012a) because of low frequency resolution of the PDS. The two remaining high frequency components were detected also in X-rays by Dobrotka et al. (2017) facilitating any discussion and interpretation. We also searched for an additional high frequency component which is of X-ray origin too (Dobrotka et al. 2019).

3.2. Fitted model

Every PDS is fitted with a multicomponent model using GNU PLOT⁴. We used the same model as Scaringi et al. (2012a), but applied it in a slightly different way. The model consists of n Lorentzian functions taken from Belloni et al. (2002)

$$p = \sum_{i=1}^n \left[\frac{c_i \Delta_i}{\pi} \frac{1}{\Delta_i^2 + (f - f_i)^2} \right], \quad (1)$$

where c_i is a constants, f_i is the searched characteristic frequency of the corresponding PDS components and Δ_i is its half-width at half-maximum. All PDSs were fitted with $n = 4$ if possible. If any component was not identified visually, or the fitting process did not yield a satisfying result,

² We use power normalized by the total variance according to Horne & Baliunas (1986). Since the normalization does not affect the shape of the PDS, this has no importance in our case.

³ If the number of averaged log-log periodogram points per bin is lower than the selected value of 30 (3 points from each of 10 periodograms), the bin is larger until the condition is fulfilled. This happens for lowest frequencies. The motivation is to get enough points for mean value with error determination.

⁴ <http://www.gnuplot.info/>

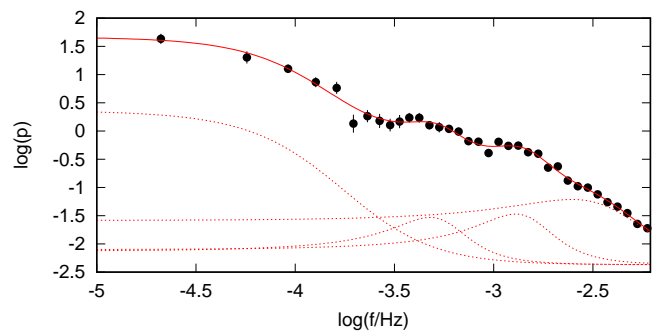


Fig. 2. Example of individual Lorentzian components (red dashed line) from Equation (1) yielding a multicomponent shape of the fit (red solid line). While the fitting is performed in $\log(p)$ vs f , the individual PDS "humps" are better seen in $\log(f \times p)$ vs $\log(f)$ (see such equivalent in Fig. 4, day 110-120).

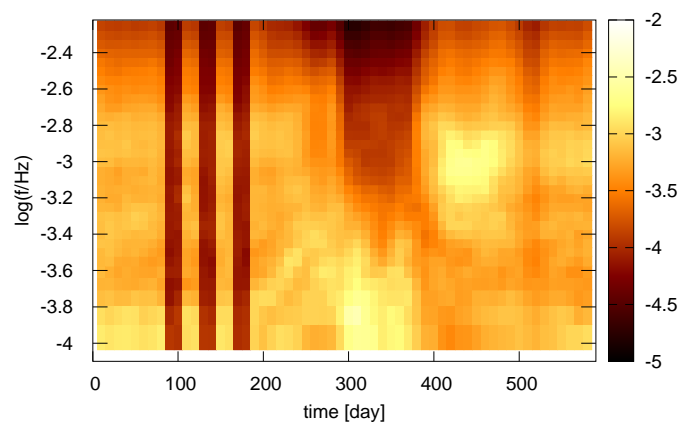


Fig. 3. PDS evolution as a function of time with y-axis units of $\log(f \times p)$. The color/gray scale represents the normalized Lomb-Scargle power. The three vertical dark bands are gaps due to too large gaps in the data. The map is slightly smoothed.

we reduced the number of components up to $n = 2$. Usually the fourth (lowest) Lorentzian fitting the lowest frequency part converged to a very low value of f_i and described the rising or constant power toward lowest frequencies. This component is not of our interests and is used just to describe continuously the whole PDS (Fig. 2).

Finally, when fitting the PDSs we used the averaged $\log(p)$ instead of p (described above). All subsequent PDSs are better visualized in $\log(f \times p)$ as y-axis units. Such visualization is suitable in the case of steep red noise, where individual components are better seen which simplifies the characteristic frequencies identification needed for the number of components set up and initial parameter estimate.

3.3. Results

The power of individual frequencies is depicted as an evolution map in Fig. 3, with some examples shown in Fig. 4. The decrease of the high frequency power during the low state is clear, while the power rises below approximately $\log(f/\text{Hz}) = -3.4$. Moreover, another strong power increase at approximately $\log(f/\text{Hz}) = -3$ after the minimum is noticeable too.

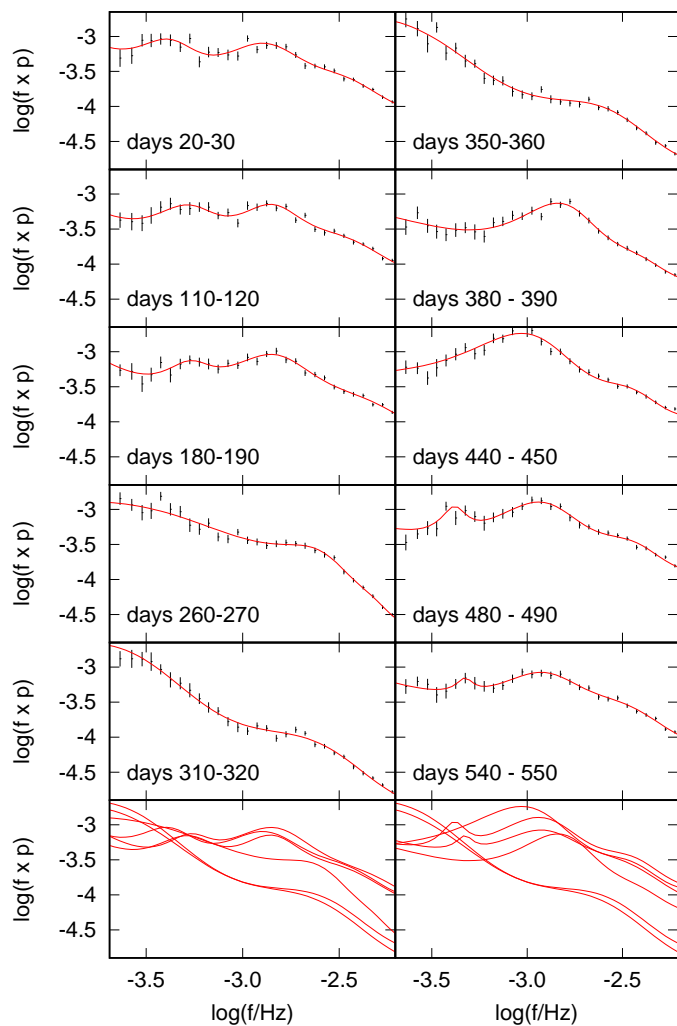


Fig. 4. Some representative examples of the calculated PDSs (small vertical lines as errors of the mean) with corresponding fits (red lines) in $f \times p$ as y-axis units. Two different cases are shown, i.e. transitions from the high to low state (left panels) and vice versa (right panels). The (middle) time locations of the PDSs are marked as red arrows in the lower panel of Fig. 1. All displayed fits are directly compared in the bottom panels (both panels comprise days 310-320 and 350-360 for comparison).

For further analysis and discussion of the PDS evolution we selected only the best and well resolved fits of clear PDS components, i.e. we selected PDS frequencies with errors $\delta \log(f_i) < 0.2$. All bad or poor fits yield large errors due to large PDS data scatter. Individual frequencies f_i are depicted in upper panel of Fig. 1.

Three distinct frequencies before and after the minimum are noticeable. While these values seem to be stable during the high state, the frequencies are variable during the transition. During the latter the f_1 component is missing. As seen in Fig. 4 the PDS dramatically changes in shape in this dynamic stage, i.e. it becomes steep with hardly resolvable components. Therefore, it is not sure whether the components disappeared or their powers just become too small to be resolved. Moreover, two low frequency points at $\log(f/\text{Hz}) = -3.54$ and -3.61 (days 235 and 405, respectively) appears during the transitions. Whether these belong to f_1 or they are independent components is hard to conclude because of a small number of fitted frequencies.

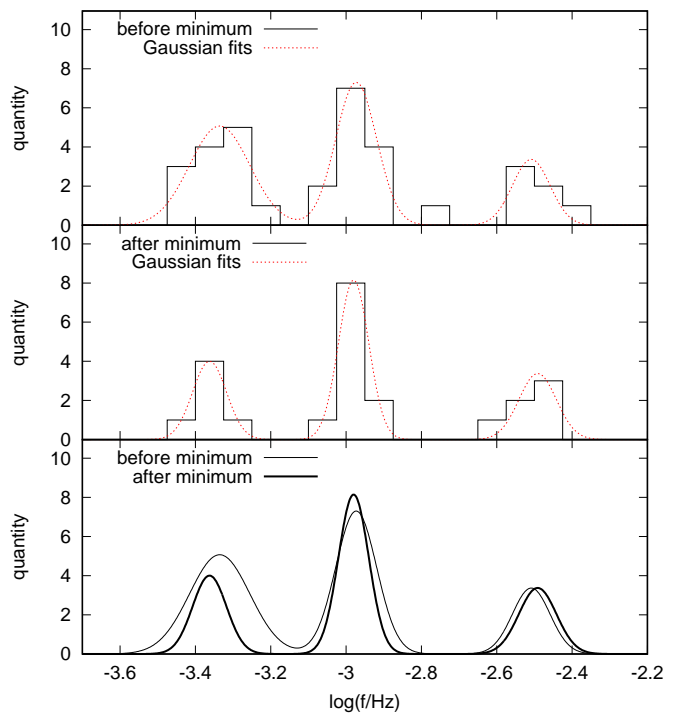


Fig. 5. Histograms of measured frequencies from the upper panel of Fig. 1 (points in the shaded areas are used). Multi-components Gaussian fits are shown and compared in the bottom panel.

Table 1. Mean values with $1\text{-}\sigma$ parameters as error estimates of the frequencies from Fig. 1 before and after the low state (marked as gray areas in Fig. 1).

position	$\log(f_1/\text{Hz})$	$\log(f_2/\text{Hz})$	$\log(f_3/\text{Hz})$
before	-3.34 ± 0.08	-2.97 ± 0.05	-2.51 ± 0.05
after	-3.36 ± 0.05	-2.98 ± 0.04	-2.49 ± 0.05

Helpful is the evolution map in Fig. 3 where a clear line is seen to rise from $\log(f/\text{Hz}) = -3.8$ to -3.6 between days 200 and 300. This suggests, that the two deviated low frequency points represent an independent component with frequency lower than f_1 .

The distribution of frequencies before and after the transition is well described by histograms in Fig. 5. We fit individual cases with a multi-Gaussian model with three components. The fitted mean values with $1\text{-}\sigma$ as errors are summarized in Table 1. Direct comparison of the fits (bottom panel of Fig. 5) suggests that after the minimum all frequencies gain their pre-minimum values.

We did not do the same histogram study for the low state because the points suggest variable behaviour. Just at the beginning of the brightness fall all three components start to deviate toward higher frequencies suggesting systematic variability (marked as blue arrows in Fig. 1). The trend continues toward day 300 after which the detection of individual PDS components was very problematic or even impossible.

There are two interesting points during the low state in Fig. 1. One is at day 290. It does not follow the increasing trend of f_2 , but jumps below other measurements. This point corresponds to a local re-brightening marked as vertical dashed arrow. Probably this opposite brightness be-

haviour corresponds to opposite frequency evolution. The other deviated point is during the day 320. It appears like pre-minimum f_2 value, but this can be also f_1 component which evolved to such a high value (at the end of the corresponding blue arrow). After the low state, all frequencies return back to the pre-minimum level.

4. Superposed shot profile analysis

The PDS is a very generalized technique, and various structures with the same/similar characteristic frequency can blend together and form a single PDS feature. This is the case of the dominant PDS feature at $\log(f/\text{Hz}) = -3$. Dobrotka et al. (2019) performed a superposed shot profile analysis (method based on Negoro et al. 1994) of the fast variability, and found that both the central spike and side lobes produce a PDS pattern very close to $\log(f/\text{Hz}) = -3$. If this PDS component is variable, the standard PDS study can not resolve substructures of which the shot profile is responsible for the variability.

4.1. Method

Therefore, as an additional study of the variability morphology we performed the same superposed shot profile analysis as in Dobrotka et al. (2019). The goal is to "see directly" individual PDS components in the flare shape like in the case of Cyg X-1 (Negoro et al. 2001). The method has three steps. First is the shots/flares identification. A light curve point is identified as a peak, if N_{pts} points to the left and N_{pts} points to the right have lower fluxes than the tested point.

As a second step, the flare extension must be defined, i.e. N_{ptsext} points to the left and to the right from the peak. Like in Dobrotka et al. (2019) we used $N_{\text{ptsext}} = N_{\text{pts}}/2$ in order to not superimpose a declining branch of one flare with a rising branch of the adjacent flare, and vice versa.

As a last step after the flare selection, the flare points are averaged with maxima aligned, and resulting averaged flux minimum is subtracted from all averaged points. All flares with rare individual null points or missing data (at the edge of the light curve or gaps) were excluded from the averaging process. As discussed in Dobrotka et al. (2019) the long-term trend and barycentric correction of *Kepler* data do not affect the result.

As N_{pts} we used a value of 50. This results in 51 points (with a duration of approximately 58.8 s) per flare yielding a flare duration of 3060 s with a corresponding frequency of $\log(f/\text{Hz}) = -3.49$. This is enough to visualize the studied frequency interval in the previous section.

For a superposed shot profile we used 10 equally spaced subsamples of the whole light curve as shown by the vertical blue lines in Fig. 1. This results in enough flares for averaging and we can visualize the rough time evolution. A larger number of light curve subsamples would yield to a smaller number of flares per average resulting in higher noise and lower resolution.

Finally, Scaringi et al. (2017) investigated a part of the same data (during the low state) and found a quasi-periodic signal present only during the very faintest period of time when the light curve reaches a roughly constant minimum brightness level. The authors call this state a deep low state. They present a scenario in which this non-magnetic CVs

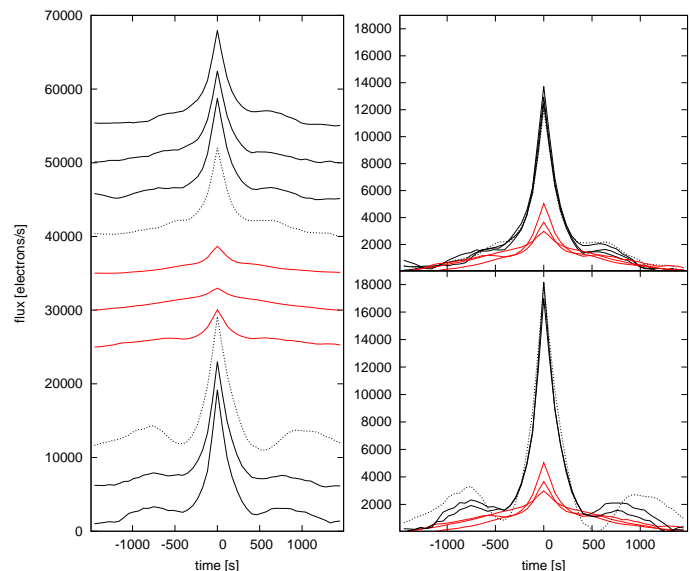


Fig. 6. Averaged shot profile time evolution. Black solid lines represent shot profiles during the high state, the black dotted lines are the profiles during both transitions, and the red solid lines represent the low state. Left panel - profiles vertically offset with time elapsing from up to down. Right panels - direct comparison/superposition of profiles showing accession to the low state (upper panel), and ascension from the low state (lower panel).

undergoes a short lasting regime of magnetically driven accretion causing the quasi-periodic bursts. In order to not contaminate the average profile with other burst-like patterns, we excluded the deep low state from the analysis. This data interval between days 299 and 315 is marked as dark shaded area in the lower panel of Fig. 1. The QPOs have a shape of 30 min bursts repeating every 2 hours. The corresponding frequencies are $\log(f/\text{Hz}) = -3.86$ and -3.25 . The upper panel of Fig. 1 does not show any point at these frequencies during the problematic part, therefore the PDS is not affected.

4.2. Results

Resulting shot profiles with a central spike and side-lobes like in Dobrotka et al. (2019) are shown in Fig. 6. During the transition from the high to low state (upper right panel) all components amplitudes just decrease, with side-lobes being non-detectable at the end. During the transition from the low to high state (lower right panel) the behaviour is reverse, and the central spike gets higher amplitude compared to the pre-minimum stage. While its amplitude increases and remains more or less stable after the transition, the amplitude of the side-lobes culminates toward the end of the transition phase (dotted line). The latter probably corresponds to the enhanced power of the f_2 component at the end of the transition phase seen in Fig. 3 or in Fig. 4 as days 440-450. This is the information not provided by the standard PDS method, i.e. different shot profile substructures with the same/similar characteristic frequency behaving differently blends into a single PDS component.

5. Discussion

We studied the PDS evolution of MV Lyr before, during and after the low state captured by the *Kepler* satellite. We focused our study on frequencies detected in previous PDS analysis by Scaringi et al. (2012a). We used a slightly different method than the authors in order to reduce the PDS scatter. We averaged/binned the periodograms in log-log space with a constant logarithmic frequency step if a minimum number of averaged periodogram points per bin is satisfied. The latter reduces the resolution at low frequencies. Therefore, we were interested only in PDS components with highest frequencies.

5.1. Phenomenology

All PDS components are probably present in both the high and low states with variable values during the transition and low state. The two highest components show significant increase in frequency. The lowest frequency component is problematic to detect in the low state, but if present, it increases in frequency too. The power above $\log(f/\text{Hz}) = -3.4$ strongly decreases during the transition to the low state, while it significantly increases for lower frequencies. This different behaviour suggests different physical origin of the variability below and above $\log(f/\text{Hz}) = -3.4$.

The characteristic frequency variability during the transition suggests the correlation of the frequencies with the flux. However, after the system returns back into the high state, the flux rises continuously while the frequency values are stable. Therefore, the frequencies depend on the activity stage and not the flux. This may be expected, because if the disc is fully reconstructed after the low state, no additional structural changes are generated by the increasing mass accretion rate. The idea is that the characteristic frequencies depend on the accretion flow structures (reconstructed and stable after the minimum), while the flux is proportional to the mass accretion rate (still rising after the minimum).

5.2. Physical model

5.3. Varying inner disc radius

The presence of PDS components in various accreting systems motivates many authors to connect the frequency values with physical parameters of that system. For example the connection of black hole mass with a PDS break frequency in active galactic nuclei is such case (see e.g. González-Martín & Vaughan 2012, Mohan & Mangalam 2014). This should be the result of different inner disc radii being a function of the black hole mass. In CVs the PDS components can be connected to the inner disc radius too (Balman & Revnivtsev 2012). The luminosity of these binaries is dominated by the release of gravitational potential energy of the gas in the disc, and therefore the brightness is directly connected to the mass accretion rate. The sudden drop in brightness in MV Lyr or VY Scl binaries (see Warner 1995 for a review) means that the mass accretion rate decreases considerably. The mass transfer can fall from more than $10^{-8} M_{\odot} \text{y}^{-1}$ to less than $10^{-11} M_{\odot} \text{y}^{-1}$ (Scaringi et al. 2017). The latter is typical for a dwarf novae in quiescence. Following the disc instability model (see Lasota 2001 for a review) the disc is truncated during such a low state, while it is fully reformed down to

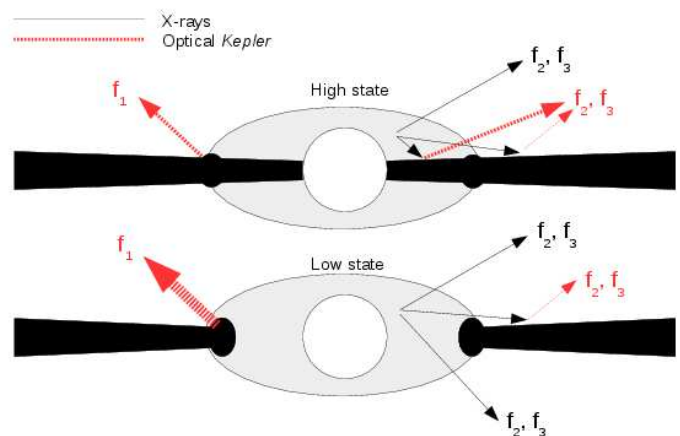


Fig. 7. Visualization of the proposed scenario, where f_2 and f_3 components are generated in the hot corona as X-ray radiation which is reprocessed into optical by the underlying thin disc. The thickness of the arrows represents the radiation intensity. See text for details.

the white dwarf surface in the high state. Therefore, during the transition from the high to low state studied in this paper, the inner disc must recede to larger radii. This is the basic idea of Balman & Revnivtsev (2012) who suggest that the characteristic frequency of a PDS component generated at the inner disc radius must decrease simultaneously. However, the variability of all components in this paper shows an opposite behaviour. This suggests that the mentioned correlation of the characteristic frequencies with the inner disc radius is not applicable.

5.4. f_2 , f_3 components and reprocessing model

Another explanation of the observed behaviour is based on the model proposed by Scaringi (2014). Following the author the f_2 component is generated by an inner geometrically thick disc, the so called X-ray corona. This disc radiates in X-rays, which are subsequently reprocessed into optical by the inner geometrically thin disc. Dobrotka et al. (2017) confirmed the X-ray origin of this PDS component, which supports the corona origin. Moreover, the f_3 component is of X-ray origin too (Dobrotka et al. 2019). If the thin disc is reprocessing the X-rays into optical, the recession of this disc during the low state means lower reprocessing surface. This can result in optical flux decrease while the frequencies are unchanged (Fig. 7). The variation of the latter can be generated by the transforming corona due to changing mass accretion rate.

Another aspect is the X-ray emissivity. During the high state only a small fraction of the flow is evaporated into the corona. The mass accretion rate based on a cooling flow model yields only $7 \times 10^{-12} M_{\odot} \text{y}^{-1}$ (Dobrotka et al. 2017). This is typical value of the mass accretion rate in the low-state of this class of objects (see e.g. Gänsicke et al. 1999), when the central disc is truncated and the whole mass flow is evaporated into the corona (Fig. 7). The X-rays are generated by free-free transitions and the emissivity is proportional to n^2 , where n is the plasma density. If the mass accretion rate (or n) through the corona is the same (unchanged) during both the high and low states, the gravitational energy liberation does not vary. This results in unaltered amplitude of the variability, and no PDS power

decrease due to emissivity is expected. Apparently, this is not observed as shown in this paper. Therefore, additional physical process (ex. reprocessing) affecting the variability is expected.

Finally, the temporal higher power of the f_2 component after the minimum is interesting. During the disc redevelopment the propagating increase of the mass accretion from outer disc regions pushes the inner disc edge toward the white dwarf. Such a mass wave can enhance specific variability in the corona, which returns to the initial pre-minimum stage after relaxation/stabilization of the flow.

5.5. Energetic aspect of the reprocessed X-rays

The reprocessing scenario is attractive, but some energy based test is worth to do. For this purpose we used *XMM-Newton* OM data presented in Dobrotka et al. (2017) because these data are well calibrated, while the *Kepler* case is more problematic. After transforming the OM light curve taken with UVW1 filter into fluxes, the amplitude of the variability represented by the root square of the variance is of 2.3×10^{-14} ergs/s/cm/Å. Assuming the same flux in the whole optical band we get a rough estimate of the integrated optical flux. However, this is merely an upper limit because it is well known that the flickering has higher amplitude toward higher energies. So in reality, the amplitude should decrease toward lower energies. Lets suppose that the wavelength interval of our assumed "optical" band is between 2500 and 7000 Å (limits of UVW1⁵ and V filter). Multiplying the UVW1 flux with the length of this band (4500 Å) we get the integrated flux of 1.4×10^{-10} ergs/s/cm, i.e. due to roughness of the estimate we take $\sim 10^{-10}$ ergs/s/cm. Moreover, Dobrotka et al. (2017) mention that the *Swift* flux in the interval of 0.2 - 10 keV is approximately 5.4×10^{-12} ergs/s/cm, i.e. approximately 20 times less than the estimated optical flux upper limit. This makes the reprocessing scenario energetically insufficient.

We do not expect that the radiation outside the 0.2 - 10 keV range contributes significantly to the overall X-ray flux. Therefore, the estimated X-ray flux is at its maximum. In order to get both energy bands closer, more realistic estimate of the optical flux is the only possibility. Some reduction of the latter can be achieved when accounting for decreasing flux toward lower energies. If we assume that the flickering amplitude decreases linearly, and reaches zero value at the lower energy limit of the V filter⁶, the reduction factor is 2. This does not resolve the energy insufficiency, it only decreases the band ratio from 20 to 10.

Another aspect is the time scale of the flickering variability. Scaringi (2014) modeled only the f_2 frequency, and identified the corona as the variability source. Therefore, in such case the reprocessing generates only the optical f_2 signal, and the lower frequency components can be generated by the accretion disc itself. Therefore, in order to get correct energy estimate, the lower frequencies must be excluded from the flickering. For this purpose we detrended the OM light curve from Fig. 1 in Dobrotka et al. (2017)

⁵ Using lower energy filters like U or B starting at 3000 or 3500 Å instead of UVW1 does not change the following energetic discussion.

⁶ This allows some amplitude to be observable also in the R band.

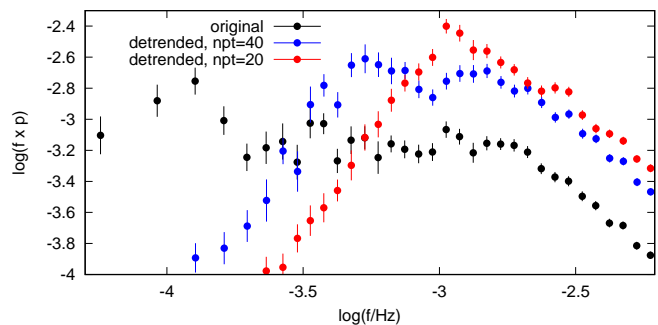


Fig. 8. PDSs from the first 10 days of *Kepler* data. Compared are the original case with two PDSs calculated from data after detrending using running median. npt represents the number of median window points.

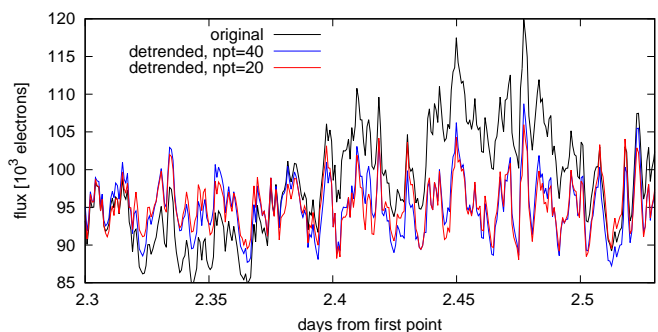


Fig. 9. Snapshot of the *Kepler* light curve compared with the detrended cases after removing the running median. The low frequency variability not present in the red and blue curves is clear. Parameter npt has the same meaning as in Fig. 8.

using running median. Using 20 adjacent points⁷ for the running window from which the median is calculated, the f_2 feature is still dominant in the PDS. The corresponding amplitude of the variability is approximately 1.5 times lower. Such reduction of the variability amplitude is again not a solution, and it only decreases the band ratio from 10 to approximately 7. A lower number of points per median window already affects the dominant f_2 PDS feature, and therefore any further reduction of the variability amplitude is not possible.

The *Kepler* case is negligibly better. In Fig. 8 we show the original and detrended PDSs of first 10 days. Detrending using 40 and 20 points per median window reduces the variability amplitude by a factor of approximately 1.8 and 2, respectively (Fig. 9). Apparently, all "attempts" how to reduce the optical flux are insufficient, and all estimates are still one order of magnitude larger than the estimated X-ray flux.

Apparently, we have a serious inconsistency between interpretation and energies. The clue is in an exact understanding of the variability components. Relying only on PDS, we study one f_2 pattern. But the shot profile studied in Section 4 and in Dobrotka et al. (2019) identify two f_2 components which blend and are non-distinguishable in standard PDS study. We propose a model, where the inner disc mass accretion fluctuations are somehow correlated

⁷ 10 points to the left, 10 to the right from the corrected point. This yields time scale of 1050 s (including the corrected point) with the OM light curve cadence of 50 s, which corresponds approximately to the frequency f_2 .

with the fluctuations in the corona. The inner disc generates its own high amplitude f_2 pattern, while the corona generates a low amplitude f_2 pattern by reprocessing. Such high amplitude pattern can be the central spike seen in Fig. 6, while the low amplitude patterns can be the side lobes. Inspecting the amplitudes from Fig. 5 in Dobrotka et al. (2019) we find that the side lobe amplitudes are lower than the peak one by factors of 8 and 9.2 for the left and right side lobe, respectively. Taking the profiles from Fig. 6, the factors are comparable except the one with clearly enhanced side lobes. This reduces the corresponding optical flux by one order of magnitude, making the energetic ratio satisfied and suitable for the reprocessing scenario.

Finally, the corona is an evaporation of the underlying thin disc, and any mass accretion fluctuation of this thin disc must result in modulation of the mass evaporation. Such fluctuations in evaporation can modulate and trigger mass accretion fluctuations in the corona. This is the above assumed disc-corona correlation.

5.6. Low frequency components

The behaviour of the f_1 component during the low state is enigmatic because of poor statistics. However, strong power rise toward lower frequencies is noticeable. Whether it represents the shifting f_1 is not sure, but certainly it suggests increasing activity below f_1 . Not reacting to inner disc recession like f_2 and f_3 suggests that the origin of this power rise must be searched elsewhere. Some outer disc region with possible enhanced activity during the low state must be a source. For example the disc-corona interaction (Fig. 7) at the corona outer edge can be a solution.

Such a more active region can be a source of QPOs generated by rotational motion of accretion inhomogeneity. This rotation would generate variabilities on a dynamical time scale

$$t_{\text{dyn}} \sim \left(\frac{R^3}{GM_1} \right)^{1/2}, \quad (2)$$

where G is the gravitational constant, M_1 the primary mass and R the distance from the center. Using $M_1 = 0.73 M_\odot$ (Hoard et al. 2004) $t_{\text{dyn}} = 72$ or 580 s for $R = 8 \times 10^9$ and 32×10^9 cm, respectively. The former is the corona radius derived by Scaringi (2014), while the latter is a disc radius estimate from Dobrotka et al. (2015). Corresponding frequencies of $\log(f/\text{Hz}) \sim -2.8$ and -1.9 are too high for f_1 or lower values. However, the value of -2.8 is close to $\log(f_2/\text{Hz}) \sim -3.0$ component in the high state. But from Scaringi (2014) and Dobrotka et al. (2017) we know that viscous process in the geometrically thick X-ray corona is the probable source in this case.

Since we study the disc reconfiguration driven by viscous processes, similar estimate can be done for the viscous time scale

$$t_{\text{visc}} \sim \frac{t_{\text{dyn}}}{\alpha(H/R)^2}, \quad (3)$$

where α is the basic disc parameter by Shakura & Sunyaev (1973) and H is the height scale of the disc. Some examples of the corresponding frequencies as a function of R are shown in Fig. 10. The values are calculated from the white dwarf surface estimated following Nauenberg (1972) up to the outer disc edge of 32×10^9 cm. The vertical dotted line

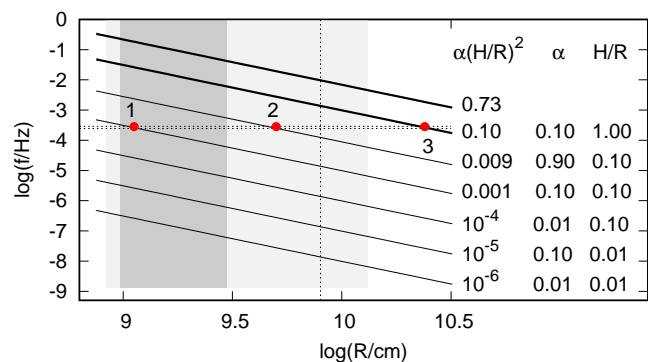


Fig. 10. Frequencies corresponding to viscous time scale compared to the two lowest measured frequencies from Fig. 1 (two horizontal dotted lines). Various models with different parameters listed as labels are shown. The vertical dotted line is the corona radius from Scaringi (2014). The shaded areas are the inner disc radius intervals from Fig. 4 of Scaringi et al. (2017). Labeled points are solutions showing the measured frequencies.

shows the corona radius from Scaringi (2014). Various combinations of α and H/R are shown. Apparently, compared to the horizontal dotted lines showing the frequencies of $\log(f_1/\text{Hz}) = -3.54$ and -3.61 (lowest values from Fig. 1), large range of $\alpha(H/R)^2$ is possible, i.e. from 0.001 to 0.1 shown as 3 solutions (points 1, 2, 3) yielding $H/R \geq 0.1$. This suggests that the source is no longer a geometrically thin disc. The solutions range from (point 1) an inner radius disc derived by Scaringi et al. (2017) using maximum possible constrains (dark shaded area in Fig. 10) up to (point 3) a radius larger than the coronal radius derived by Scaringi 2014. Therefore, we are not able to quantify the source characteristics, only conclusion is that the geometrically thick corona is a potential solution.

Other disc structures can be still candidates for the low frequency components. A hot spot or stream (from the secondary) overflow are also localized further away from the central disc. The superhump interpretation would be also possible, but the discussed frequencies $\log(f/\text{Hz}) = -3.54$ and -3.61 are far from the superhump case of $\log(f/\text{Hz}) = -4.08$ derived by Borisov (1992) and Skillman et al. (1995). Only direct X-ray observation can bring final answer. Crucial is to determine whether f_1 is of X-ray origin like f_2 and f_3 , and how is the PDS power compared to the high state. If detected in X-rays, this would exclude any stream overflow, hot spot or superhump scenario, and places the radiation source into central regions like a corona or boundary layer.

5.7. Analogy with X-ray binaries

The presence of PDS components in *Kepler* data of CVs at frequencies close to the values determined in this paper is not new. Dobrotka & Ness (2015) and Dobrotka et al. (2016) studied PDSs of two dwarf novae present in the *Kepler* field, i.e. V1504 Cyg and V344 Lyr. Both systems show similar behaviour of the PDSs in dependence of the activity stage. Surprisingly not only the frequency values are comparable, but also their presence depending of the activity stage. During the low state both systems show PDS components close to f_1 , while during the high state another components close to f_2 are present.

Some other systems studied from the ground show similar low frequency components, i.e. KR Aur (Kato et al.

Table 2. List of approximate characteristic PDS frequencies in different CVs systems used for Fig. 11. The values in parenthesis are maximal (not necessary final) values of f_2 and f_3 from Fig. 1. We did not add the hypothetical highest value of f_1 (in the low state) because it is too speculative.

system	state	band	$\log(f/\text{Hz})$
MV Lyr ^a	low	optical	-3.5, (-2.5)
	low	optical	-3.6, (-2.3)
V1504 Cyg ^b	low	optical	-3.4, -2.3
V344 Lyr ^c	low	optical	-3.4
RU Peg ^d	low	X-rays	-3.5, -2.7
	low	UV	-3.3
SS Cyg ^e	low	X-rays	-2.3
	low	X-rays	-2.4
VW Hyi ^e	low	X-rays	-2.7
WW Cet ^e	low	X-rays	-2.5
T Leo ^e	low	X-rays	-2.4
MV Lyr ^a	high	optical	-3.3, -3.0, -2.5 -3.4
V1504 Cyg ^b	high	optical	-3.3, -3.0, -2.9, -2.4
V344 Lyr ^c	high	optical	-3.5, -3.0, -2.8
KR Aur ^f	high	optical	-3.4
UU Aqr ^g	high	optical	-3.8

^a this paper

^b from Table 2 of Dobrotka & Ness (2015)

^c from Table 2 of Dobrotka et al. (2016)

^d from Dobrotka et al. (2014)

^e from Balman & Revnivtsev (2012)

^f from Kato et al. (2002)

^g from Baptista & Bortoletto (2008)

2002) and UU Aqr (Baptista & Bortoletto 2008). While the former shows practically the same characteristic PDS frequency as derived in this paper, the latter is slightly lower⁸. Balman & Revnivtsev (2012) reported several high frequency components close to f_3 in X-ray data of SS Cyg, RU Peg, VW Hyi, WW Cet and T Leo. Dobrotka et al. (2014) reanalyzed the observation of the dwarf nova RU Peg during quiescence and found the multicomponent nature of the PDS with similar characteristic frequencies in UV and X-rays. Contrary to V1504 Cyg and V344 Lyr, the quiescent X-ray PDS also comprises a component between f_2 and f_3 . Perhaps more or all components are present in both stages of CVs in general, but some remains very damped during the low state. After all, the f_2 and f_3 components in MV Lyr did not disappear during the low state, just the power is very low. Because of the latter and probable variability the characteristic values are hard to be determined.

All the mentioned values are summarized in Table 2 and Fig. 11. Three distinct groups are potentially present. However, confirmation of this statement requires much larger statistical set of measured frequencies, because the histogram in Fig. 11 can be a result of a random process.

Such typical PDS components depending on brightness states are very typical for X-ray binaries (see e.g. Miyamoto et al. 1992, Miyamoto et al. 1993, Miyamoto et al. 1994 as pioneer works, or

⁸ Baptista & Bortoletto 2008 reported a presence of spiral arm and this can significantly change the nature of the variability, i.e. it may differ from the "standard" case.

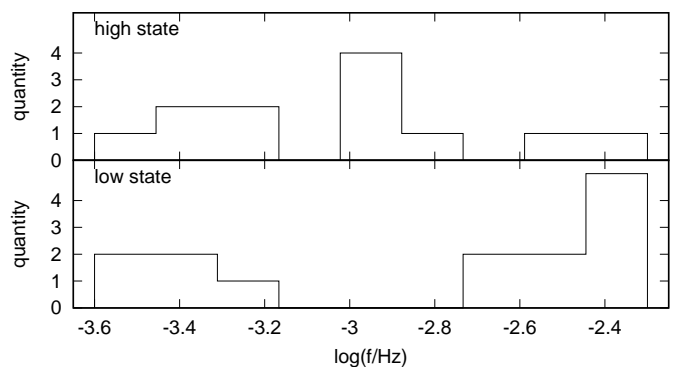


Fig. 11. Histograms of the values from Table 2. The value of -3.8 was excluded because of spiral patterns in the disc of UU Aqr making the case "non standard".

Lewin & van der Klis 2010 for a review), while it is new for CVs.

6. Summary and conclusions

The multicomponent PDS of MV Lyr shows complex transformation during the transition from high to low state and vice versa with three resolved PDS components. The high frequency part of the PDS ($\log(f/\text{Hz}) > -3.4$) considerably decreases in power during the minimum brightness compared to the high state, while the low frequency part ($\log(f/\text{Hz}) < -3.4$) significantly increases. The characteristic frequencies of the two highest PDS components increase during the low state. The same is also possible for the lowest PDS component, but with lower significance. Once the brightness starts to get back to the pre-minimum level, the frequencies returns to their pre-minimum values. Additional transient power increase of the middle PDS component at $\log(f/\text{Hz}) \simeq -3$ is clear after the minimum. The evolution of frequencies together with the overall flux suggests that the frequency values are correlated with the brightness state, and not with the flux.

The power decrease of the high frequency part of the PDS can be explained by diminishing of the receding disc surface needed for X-ray reprocessing. This is based on the knowledge that the highest PDS components are generated by the inner X-ray corona or boundary layer. However, rough estimates of the integrated optical and X-ray fluxes imply that the reprocessing scenario can not work for the whole variability, but only for its low amplitude components. Rough time scale estimate implies that the source of the lowest frequencies can be a standard disc (geometrically thicker than thin solution) embedded into the geometrically thick X-ray corona or the corona itself.

Finally, the comparison with other CV systems suggests that CVs may have common typical PDS components with similar values depending on the brightness state. This is similar to what is observed in X-ray binaries. However, larger statistical set of measurements is needed to confirm or decline this hypothesis.

Acknowledgment

AD was supported by the Slovak grant VEGA 1/0408/20, and by the Operational Programme Research and Innovation for the project : Scientific and Research Centre of

Excellence SlovakION for Material and Interdisciplinary Research“, code of the project ITMS2014+ : 313011W085 co-financed by the European Regional Development Fund. HN was supported by Grants-in-Aid for Scientific Research 16K05301 from the Ministry of Education, Culture, Sports, Science and Technology (MEXT) of Japan. We acknowledge the anonymous referee for helpful comments, particularly concerning the energetic study of the optical and X-ray flickerings.

References

- Aranzana, E., Körding, E., Uttley, P., Scaringi, S., & Bloemen, S. 2018, *MNRAS*, 476, 2501
- Balman, Ş. & Revnivtsev, M. 2012, *A&A*, 546, A112
- Baptista, R. & Bortoletto, A. 2008, *ApJ*, 676, 1240
- Belloni, T., Psaltis, D., & van der Klis, M. 2002, *ApJ*, 572, 392
- Boeva, S., Bachev, R., Tsvetkova, S., et al. 2011, *Bulgarian Astronomical Journal*, 16, 23
- Borisov, G. V. 1992, *A&A*, 261, 154
- Borucki, W. J. et al. 2010, *Science*, 327, 977
- Bruch, A. 2015, *A&A*, 579, A50
- Dobrotka, A., Mineshige, S., & Ness, J.-U. 2014, *MNRAS*, 438, 1714
- Dobrotka, A., Mineshige, S., & Ness, J.-U. 2015, *MNRAS*, 447, 3162
- Dobrotka, A., Negoro, H., & Mineshige, S. 2019, *A&A*, 631, A134
- Dobrotka, A. & Ness, J.-U. 2015, *MNRAS*, 451, 2851
- Dobrotka, A., Ness, J.-U., & Bajčičáková, I. 2016, *MNRAS*, 460, 458
- Dobrotka, A., Ness, J.-U., Mineshige, S., & Nucita, A. A. 2017, *MNRAS*, 468, 1183
- Frank, J., King, A., & Raine, D. 1992, *Cambridge Astrophysics Series*, 21
- Gänsicke, B. T., Sion, E. M., Beuermann, K., et al. 1999, *A&A*, 347, 178
- González-Martín, O. & Vaughan, S. 2012, *A&A*, 544, A80
- Hessman, F. V. 2000, *New A Rev.*, 44, 155
- Hoard, D. W., Linnell, A. P., Szkody, P., et al. 2004, *ApJ*, 604, 346
- Horne, J. H. & Baliunas, S. L. 1986, *ApJ*, 302, 757
- Kato, T., Ishioka, R., & Uemura, M. 2002, *PASJ*, 54, 1033
- King, A. R. & Cannizzo, J. K. 1998, *ApJ*, 499, 348
- Kraicheva, Z., Stanishev, V., & Genkov, V. 1999, *A&AS*, 134, 263
- Lasota, J. 2001, *New A Rev.*, 45, 449
- Lewin, W. & van der Klis, M. 2010, *Compact Stellar X-ray Sources*
- Miyamoto, S., Iga, S., Kitamoto, S., & Kamado, Y. 1993, *ApJ*, 403, L39
- Miyamoto, S., Kitamoto, S., Iga, S., Hayashida, K., & Terada, K. 1994, *ApJ*, 435, 398
- Miyamoto, S., Kitamoto, S., Iga, S., Negoro, H., & Terada, K. 1992, *ApJ*, 391, L21
- Mohan, P. & Mangalam, A. 2014, *ApJ*, 791, 74
- Nauenberg, M. 1972, *ApJ*, 175, 417
- Negoro, H., Kitamoto, S., & Mineshige, S. 2001, *ApJ*, 554, 528
- Negoro, H., Miyamoto, S., & Kitamoto, S. 1994, *ApJ*, 423, L127
- Papadakis, I. E. & Lawrence, A. 1993, *MNRAS*, 261, 612
- Sasada, M., Mineshige, S., Yamada, S., & Negoro, H. 2017, *PASJ*, 69, 15
- Scargle, J. D. 1982, *ApJ*, 263, 835
- Scaringi, S. 2014, *MNRAS*, 438, 1233
- Scaringi, S., Körding, E., Groot, P. J., et al. 2013, *MNRAS*, 431, 2535
- Scaringi, S., Körding, E., Uttley, P., et al. 2012a, *MNRAS*, 427, 3396
- Scaringi, S., Körding, E., Uttley, P., et al. 2012b, *MNRAS*, 421, 2854
- Scaringi, S., Maccarone, T. J., D’Angelo, C., Knigge, C., & Groot, P. J. 2017, *Nature*, 552, 210
- Shahbaz, T., Dhillon, V. S., Marsh, T. R., et al. 2005, *MNRAS*, 362, 975
- Shakura, N. I. & Sunyaev, R. A. 1973, *A&A*, 24, 337
- Skillman, D. R., Patterson, J., & Thorstensen, J. R. 1995, *PASP*, 107, 545
- Van de Sande, M., Scaringi, S., & Knigge, C. 2015, *MNRAS*, 448, 2430
- van der Klis, M. 1989, in *NATO Advanced Science Institutes (ASI) Series C*, Vol. 262, NATO Advanced Science Institutes (ASI) Series C, ed. H. Ögelman & E. P. J. van den Heuvel, 27
- Warner, B. 1995, *Cambridge Astrophysics Series*, 28